ELSEVIER

Journal of Volcanology and Geothermal Research 120 (2003) 249–270

Journal of volcanology and geothermal research

www.elsevier.com/locate/jvolgeores

Magma degassing and basaltic eruption styles: a case study of ~2000 year BP Xitle volcano in central Mexico

Pablo Cervantes [a], Paul Wallace [b,*]

[a] *Department of Geology and Geophysics, Texas A&M University, College Station, TX 77845, USA*
[b] *Ocean Drilling Program, Texas A&M University, College Station, TX 77845, USA*

Received 2 March 2000; accepted 1 July 2002

Abstract

To investigate the relationship between volatile abundances and eruption style, we have analyzed major element and volatile (H_2O, CO_2, S) concentrations in olivine-hosted melt inclusions in tephra from the ~2000 yr BP eruption of Xitle volcano in the central Trans-Mexican Volcanic Belt. The Xitle eruption was dominantly effusive, with fluid lava flows accounting for ~95% of the total dense rock erupted material (1.1 km^3). However, in addition to the initial, Strombolian, cinder cone-building phase, there was a later explosive phase that interrupted effusive activity and deposited three widespread ash fall layers. Major element compositions of olivine-hosted melt inclusions from these ash layers range from 52 to 58 wt.% SiO_2, and olivine host compositions are $Fo_{84–86}$. Water concentrations in the melt inclusions are variable (0.2–1.3 wt.% H_2O), with an average of 0.45 ± 0.3 (1σ) wt.% H_2O. Sulfur concentrations vary from below detection (~50 ppm) to 1000 ppm but are mostly ≤ 200 ppm and show little correlation with H_2O. Only the two inclusions with the highest H_2O have detectable CO_2 (310–340 ppm), indicating inclusion entrapment at higher pressures (700–900 bars) than for the other inclusions (≤ 80 bars). The low and variable H_2O and S contents of melt inclusions combined with the absence of less soluble CO_2 indicates shallow-level degassing before olivine crystallization and melt inclusion formation. Olivine morphologies are consistent with the interpretation that most crystallization occurred rapidly during near-surface H_2O loss. During cinder cone eruptions, the switch from initial explosive activity to effusive eruption probably occurs when the ascent velocity of magma becomes slow enough to allow near-complete degassing of magma at shallow depths within the cone as a result of buoyantly rising gas bubbles. This allows degassed lavas to flow laterally and exit near the base of the cone while gas escapes through bubbly magma in the uppermost part of the conduit just below the crater. The major element compositions of melt inclusions at Xitle show that the short-lived phase of renewed explosive activity was triggered by a magma recharge event, which could have increased overpressure in the storage reservoir beneath Xitle, leading to increased ascent velocities and decreased time available for degassing during ascent.

Keywords: basalt; eruptions; magma; volatiles; volcanology; water

* Corresponding author. Present address: Department of Geological Sciences, University of Oregon, Eugene, OR 97403, USA. Tel.: +1-541-346-5985; Fax: +1-541-346-4692.
E-mail address: pwallace@darkwing.uoregon.edu (P. Wallace).

0377-0273/02/$ – see front matter
PII: S0377-0273(02)00401-8

1. Introduction

Physical modeling of volcanic processes has clearly shown that the abundance of volatiles, primarily H_2O and CO_2, plays a major role in determining the explosivity of volcanic eruptions (Wilson, 1980; Wilson et al., 1980; Dobran, 1992; Woods and Koyaguchi, 1994). However, because the solubilities of H_2O and CO_2 in silicate melts are strongly pressure-dependent, these volatiles are largely degassed from magma during subaerial eruption, making it difficult to constrain pre-eruption concentrations. Melt inclusions trapped in phenocrysts and rapidly quenched during eruption may retain their dissolved volatiles because the host crystal surrounding the inclusion acts like a tiny pressure vessel (Lowenstern, 1995). Analyses of melt inclusions have provided valuable information on the primary volatile concentrations of a wide variety of magma types from different tectonic environments (e.g., Anderson et al., 1989; Westrich et al., 1991; Anderson and Brown, 1993; Sisson and Layne, 1993; Wallace and Gerlach, 1994; Lowenstern, 1995; Wallace et al., 1995; Sobolev and Chaussidon, 1996; Roggensack et al., 1997; Sisson and Bronto, 1998). However, it has also been recognized that low-pressure degassing during shallow-level storage at subaerial volcanoes can significantly decrease the volatile concentrations in magmas (Dixon et al., 1991) and that crystal growth in such degassed magmas can result in melt inclusions that have significantly less H_2O, CO_2, and S than undegassed magma (Wallace and Anderson, 1998).

Cinder cones are the most common type of subaerial volcano on Earth and are generally associated with lava flows (Wood, 1980). Cinder cone eruptions typically have a temporal sequence that starts with relatively rapid formation of a cinder cone during Strombolian eruptions, followed by a switch to largely effusive eruptions of lava (Walker, 1973; Gutmann, 1979; Wood, 1980; Cas and Wright, 1988). The early explosive stage may also include sustained eruptions involving ash-rich plumes that reach heights as great as 6 km above the vent, resulting in widespread ash fall deposits (Foshag and Gonzalez-Reyna, 1956). A fundamental question is whether the switch from explosive to effusive behavior reflects inherent differences in the H_2O and CO_2 contents of different batches of magma or parts of a magma chamber or whether the eruptive behavior results from processes of shallow volatile loss. For silicic eruptions, the transition from explosive to effusive eruption has been shown to be largely the result of shallow degassing (Eichelberger et al., 1986; Westrich et al., 1988; Eichelberger, 1989; Jaupart and Allegre, 1991; Westrich and Eichelberger, 1994; Woods and Koyaguchi, 1994). In cinder cone eruptions, passive effusion of voluminous lava flows (e.g., Parícutin in central Mexico) probably also requires large-scale degassing of magma before eruption; however, the explosive–effusive transition in cinder cone eruptions has not been the subject of detailed study. Volatile data on melt inclusions from basaltic to basaltic andesite eruptions in which the time-stratigraphic relations of the samples are well understood are required for understanding both low-pressure degassing processes and the dynamics of explosive basaltic eruptions. In this paper, we present data on the major element and volatile (H_2O, CO_2, S) concentrations of melt inclusions from the $\sim$2000 yr BP Xitle eruption in central Mexico. These data reveal important information on degassing during cinder cone eruptions and provide insight into the parameters that control whether eruptions are explosive or effusive.

2. Geologic setting and eruptive history

Xitle volcano is one of several hundred cinder cones in the Sierra Chichináutzin volcanic field, which is located in the central part of the Trans-Mexican Volcanic Belt (TMVB) (Fig. 1). The TMVB is an E–W-trending volcanic arc that is associated with subduction of the Cocos and Rivera Plates under the North American Plate along the Middle America Trench (Demant, 1978). The Sierra Chichináutzin volcanic field is formed by lava flows and pyroclastic products emitted from a number of small volcanic centers (Bloomfield, 1975; Martin del Pozzo, 1982). Compositions of volcanic rocks in this region range from basalt and basaltic andesite to dacite (Gunn and

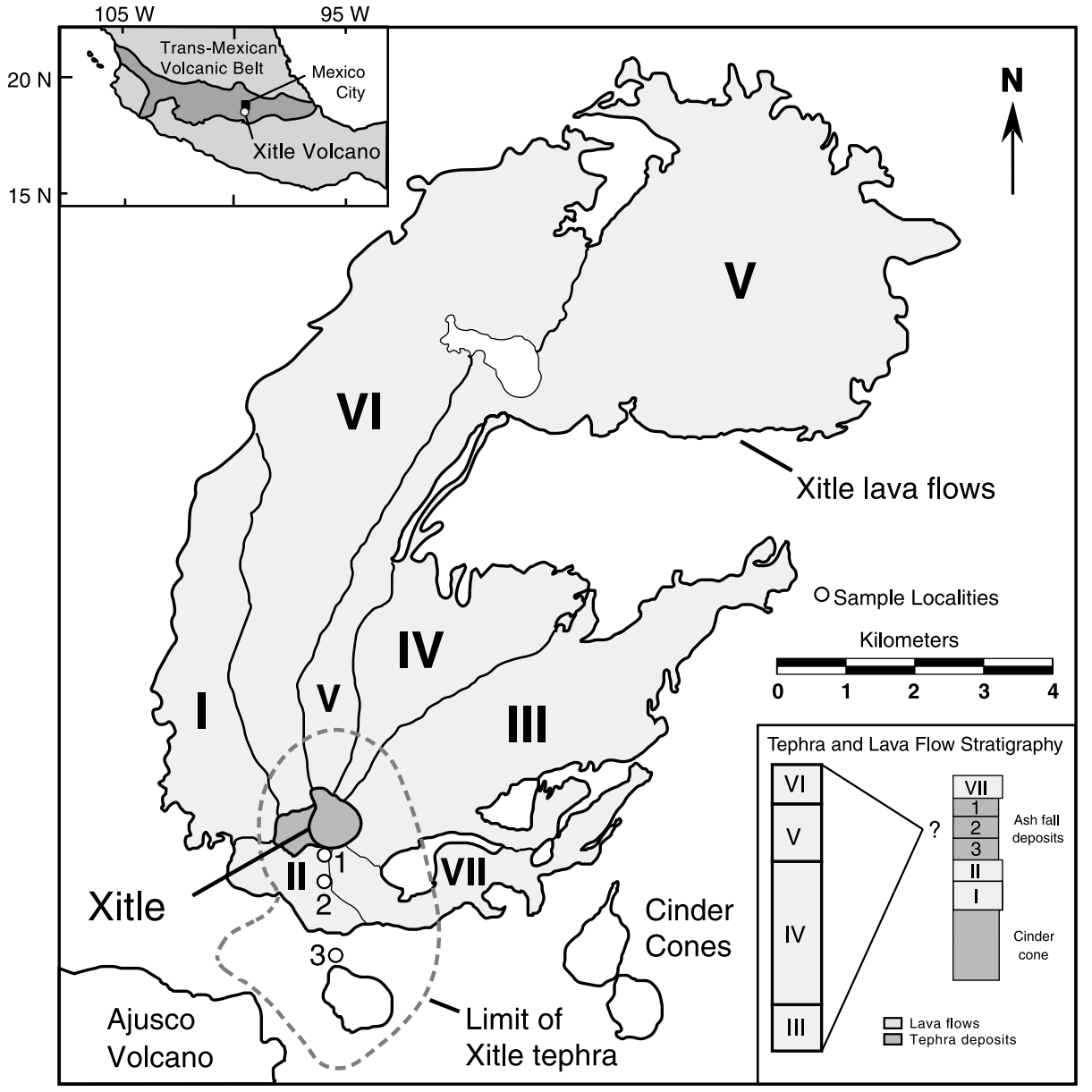

Fig. 1. Geologic map of Xitle volcano and its deposits (based on Cervantes and Molinero, 1995, and Delgado et al., 1998). The area covered by lava flows from Xitle is shown by a heavy solid line. Within this area, individual lava flows are delimited by thin solid lines and identified by Roman numerals. The distribution of tephra deposits is shown by a dashed line that corresponds to the 0.1-cm isopach. Small open circles indicate the location where the three different tephra layers were sampled and are numbered according to which layer was sampled. The inset at upper left shows the location of Xitle volcano within the TMVB (dark gray). The stratigraphic relations of the different eruptive events from Xitle are shown in the lower right corner. Two columns are shown in this inset: the right one shows the field relationships of the explosive events and the surrounding lava flows; the column to the left shows the stratigraphic relations of lava flows III–VI. The time of emplacement of tephra layers 1–3 relative to emplacement of flows III–VI is uncertain. Note that the numbering of the fall layers is contrary to the commonly used convention of numbering from base to top; we have retained this numbering to be consistent with previous studies (Cervantes and Molinero, 1995; Delgado et al., 1998).

Mooser, 1971; Wallace and Carmichael, 1999). All volcanic units of the Chichináutzin volcanic field that have been analyzed paleomagnetically show normal polarity, indicating ages less than 700 ka (Mooser et al., 1974). Within the Sierra Chichináutzin volcanic field and the TMVB as a whole, mafic lavas span a range of compositions from alkaline to calc-alkaline (Wallace and Carmichael, 1999).

Xitle volcano is located in the northern part of the volcanic field (Fig. 1), at the southern edge of Mexico City. Dating of lavas from Xitle using ^{14}C indicates an eruptive age of ~1700 (Siebe, 2000) to ~2000 yr BP (see Delgado et al., 1998). The eruption of Xitle was long considered to be the latest eruptive activity in the area. However, geochronological studies by Delgado et al. (1997) show evidence for more recent activity at nearby Pelado and Chichináutzin volcanoes. The major element compositions of lavas from Xitle include both hypersthene and mildly nepheline normative basalts (Cervantes and Molinero, 1995; Wallace and Carmichael, 1999). On a diagram of total alkalies versus silica, Xitle lavas range from alkaline to transitional in composition. Trace element abundances and ratios of key elements (e.g., Ba/Nb) suggest that the mantle source region for magmas erupted at Xitle was little affected by subducted-related enrichment, in contrast to the volumetrically dominant calc-alkaline magmas in the Sierra Chichinautzin volcanic field (Delgado et al., 1998; Wallace and Carmichael, 1999).

The eruptive stratigraphy of Xitle is the best studied of any volcano in the Sierra Chichináutzin (Cervantes and Molinero, 1995; Delgado et al., 1998). The eruption was dominantly effusive with fluid lava flows accounting for ~95% of the total dense rock erupted material (~1.1 km^3; Cervantes and Molinero, 1995). In addition to the Strombolian cinder cone-building phase, there was a later short-lived explosive phase that punctuated emplacement of lava flows. Delgado et al. (1998) divided the effusive events into seven different lava flows, where flow units V and VI are the most voluminous (Fig. 1). The explosive event consists of small ash flow deposits and three well defined ash and scoria fall deposits (Fig. 1). Field relations clearly show that the fall deposits overlie lava flow unit II and are overlain by flow unit VII (Cervantes and Molinero, 1995). However, the timing of the explosive phase relative to emplacement of flow units III–VI is uncertain (see inset in Fig. 1). The main three fall deposits have very similar distributions, suggesting that they were emplaced closely in time (Delgado et al., 1998). Interestingly, the dispersal and fragmentation characteristics of the Xitle tephra (Cervantes and Molinero, 1995) are similar to those of tephra deposits at Parícutin (Walker, 1973), although the latter eruption involved about an order of magnitude greater tephra volume.

3. Sample description

We collected material from three different sites in order to sample the three main fall deposits (layers 1–3; see Fig. 1). At the first site, a shallow pit near the north flank of the Xitle cone, we sampled the base of the deposit from the final explosive event (layer 1). At the second site, a pre-existing quarry located between the first and third sites, tephra from the middle (layer 2) and final (layer 1) explosive events were completely exposed. We collected a sample from the base of the middle layer (layer 2) at this site. To sample the base of the tephra from the first explosive event (layer 3) we selected a site in a quarry in which the distal facies of the complete sequence is exposed. The sample from layer 3 contains two different types of clasts. The first type is dense and dark gray in color, and probably represents lithic fragments. We interpret the second type, which are brownish gray in color and highly vesicular, as juvenile material. The juvenile clasts contain abundant olivine phenocrysts. At all three sampling localities, we chose clasts ≤ 3 cm in diameter to ensure that the samples had cooled rapidly enough during eruption to quench melt inclusions to glass.

4. Methods

4.1. Sample preparation

For each tephra sample, we sieved ~300 g of

material to obtain the size fraction (0.355–1.4 mm) that contained loose olivine crystals. Crystals in this size fraction were handpicked using a binocular microscope. Clasts in the coarse fraction (1.4 mm–3 cm) were gently crushed using a ceramic mortar in order to separate olivine crystals from the matrix glass. Olivine crystals were handpicked from the crushed clasts.

The crystals were placed in immersion liquid (refractive index 1.678) in order to select crystals with melt inclusions for analysis. The crystals with the largest and best preserved inclusions were separated, and morphological and textural characteristics were noted before sectioning (Table 1). To prepare samples for quantitative infrared spectroscopic analysis, double-polished wafers were prepared from melt-inclusion-bearing crystals so that both faces of the wafer intersect the inclusion.

Melt inclusions within the olivine wafers were analyzed by Fourier transform infrared (FTIR) spectroscopy. The thickness of each crystal wafer was measured using a petrographic microscope (10× objective) with a calibrated ocular. In order to view the melt inclusion under the microscope, the edge of the wafer was glued to a needle with epoxy and then placed in a well filled with immersion liquid. The precision of the thickness measurements varies from ±1 to ±3 μm depending on the proximity of a given inclusion to the edge of the wafer. After FTIR analyses were completed and sample thicknesses measured, the melt inclusion samples were prepared for electron microprobe analysis.

4.2. Infrared spectroscopy

The dissolved H_2O and CO_2 contents of the melt inclusion glasses were measured by infrared spectroscopy using a Nicolet Magna 560 FTIR spectrometer interfaced with a Spectra-Tech NicPlan microscope in the Department of Geology and Geophysics at Texas A&M University. A KBr beamsplitter and liquid nitrogen-cooled $HgCdTe_2$ detector were used for all spectra. The quantitative procedures and band assignments described in Dixon et al. (1995) were followed for this work. Quantitative measurements of dissolved total H_2O, CO_2, molecular H_2O, and OH were determined using Beer's law:

$$c = \frac{MA}{\rho l \varepsilon}$$

where c is the concentration in weight fraction of the absorbing species, M is the molecular weight (18.02 for total H_2O, molecular H_2O, and OH and 44.00 for CO_3^{2-}), A is the absorbance of the band of interest, ρ is the room temperature density of the glass (2800 kg/m^3 assumed for all inclusions), l is the sample thickness (path length), and ε is the molar absorption coefficient.

Total dissolved H_2O was measured from the intensity of the broad, asymmetric band centered at 3530 cm^{-1}, which corresponds to the fundamental OH-stretching vibration (Nakamoto, 1978), using an absorption coefficient of 63 ± 3 l/mol cm (Table 2; Dobson et al., unpublished data, cited in Dixon et al., 1995). Molecular H_2O and OH (Table 2) contents were calculated from the absorbances of the bands at 5200 cm^{-1} and 4500 cm^{-1}, respectively. Molecular H_2O contents were also calculated from the absorbance of the band at 1630 cm^{-1}.

Dissolved CO_2 was measured using the peaks at 1515 and 1430 cm^{-1}, which correspond to antisymmetric stretching of distorted carbonate groups (Dixon et al., 1995). Because the shape of the background in this region is complex (Dixon et al., 1995) the spectrum of a reference sample with similar composition and no measurable carbonate was subtracted from the spectrum of the measured sample to obtain a relatively flat background (Table 3).

Absorption coefficients for the 1430, 1515, 1630, 4500, and 5200 cm^{-1} bands in basaltic glass are compositionally dependent (Dixon and Pan, 1995). Using the major element compositions of the Xitle melt inclusions as measured by electron microprobe, we calculated absorption coefficients using the linear equations reported in Dixon and Pan (1995) and Dixon et al. (1995). The calculated absorption coefficients were 266 ± 18 l/mol cm for the 1515 and 1430 cm^{-1} doublet (carbonate), 40 ± 4 l/mol cm for the 1630 cm^{-1} band (molecular H_2O), 0.80 ± 0.09 l/mol cm for the 4500 cm^{-1} band (OH), and 0.99 ± 0.11 l/mol cm for the 5200

Table 1
Textural characteristics of analyzed melt inclusions from Xitle volcano

Inclusion	Shape	Type	Size (μm)	Vapor bubble diameter (μm)	Vapor bubble (vol.%)	Texture	Crystals
Layer 1							
X1-2	Irregular	Hourglass	250×100	40	1.3	Glassy, wrinkled	Small, scarce
X1-4	Irregular	Fully enclosed	175×175	–	–	Glassy, wrinkled	Present
X1-5	Irregular	Reentrant	360×170	135×105	3.1	Devitrified	None
X1-7	Irregular	Fully enclosed	400×150	–	–	Glassy	Small, scarce
X1-8	Irregular	Fully enclosed	220×180	90	6.2	Glassy	Small, scarce
X1-9	Irregular	Reentrant	410×250	50	0.1	Glassy, wrinkled	Small, scarce
X1-10	Irregular	Fully enclosed	330×340	–	–	Glassy, wrinkled	Small, scarce
X1-11	Irregular	Fully enclosed	550×430	80	1.5	Glassy, wrinkled	Small, abundant
X1-12	Irregular	Reentrant	450×150	–	–	Glassy	Small, abundant
X1-13	Irregular	Hourglass	410×450	–	–	Devitrified	Small, abundant
X1-14	Irregular	Reentrant	440×650	70	0.8	Glassy	Small, abundant
X1-15	Irregular	Reentrant	350×50	–	–	Glassy, wrinkled	Small, scarce
Layer 2							
X2-1	Ellipsoidal	Fully enclosed	165×132	–	–	Glassy, wrinkled	None
X2-2	Irregular	Fully enclosed	270×240	–	–	Glassy, wrinkled	None
X2-4	Irregular	Fully enclosed	325×235	80	1.6	Glassy	None
X2-5	Ellipsoidal	Fully enclosed	260×135	–	–	Glassy	None
X2-6	Irregular	Fully enclosed	285×220	–	–	Glassy	Small, scarce
X2-7	Irregular	Hourglass	205×125	–	–	Glassy	Small, abundant
X2-8	Irregular	Hourglass	415×350	110	4.3	Glassy, wrinkled	Small, abundant
X2-9	Irregular	Hourglass	160×130	45	1.9	Glassy, wrinkled	None
X2-10	Irregular	Hourglass	310×355	–	–	Glassy	Small, abundant
X2-11	Ellipsoidal	Fully enclosed	195×130	–	–	Glassy, wrinkled	Small, scarce[a]
X2-12	Irregular	Fully enclosed	270×160	90	4.6	Glassy, wrinkled	None
X2-14	Irregular	Reentrant	572×210	100	1.5	Glassy	Large, scarce
X2-17	Irregular	Fully enclosed	510×170	105	3.4	Glassy	Large, scarce
X2-18	Irregular	Fully enclosed	420×240	–	–	Glassy	Large, scarce
X2-19	Irregular	Reentrant	245×165	–	–	Devitrified	Small, abundant
X2-20	Irregular	Reentrant	910×610	95	2.7	Glassy	Small, abundant
X2-21	Irregular	Reentrant	510×270	75	2.3	Devitrified	Small, abundant
Layer 3							
X3-1	Irregular	Reentrant	260×200	–	–	Glassy	Small, abundant
X3-2	Irregular	Hourglass	310×110	–	–	Devitrified	Small, abundant
X3-3	Irregular	Fully enclosed	280×230	–	–	Glassy, wrinkled	Large, scarce
X3-4	Irregular	Fully enclosed	240×170	–	–	Glassy	Small, scarce
X3-5	Irregular	Fully enclosed	270×160	–	–	Glassy	Small, abundant
X3-6	Irregular	Fully enclosed	360×170	75	2.8	Glassy	Small, abundant
X3-8	Irregular	Fully enclosed	730×150	–	–	Glassy	Small, abundant
X3-9	Irregular	Fully enclosed	360×130	80	10.1	Glassy	Small, scarce

Shape: Indicates the original shape of the inclusion before sample preparation.
Type: Fully enclosed indicates that the inclusion is completely surrounded by the olivine host. Reentrant indicates that the inclusion is connected to the exterior of the host crystal. Hourglass indicates that the inclusion is connected to the outside of the host by a thin melt (glass)-filled capillary.
Size: Melt inclusion dimensions given as maximum dimension and dimension perpendicular to the maximum.
Vapor bubble diameter: Diameter of vapor bubble, if present in inclusion. Most bubbles were spherical. For ellipsoidal bubbles, the average of the dimensions is given.
Texture: Glassy for inclusions that are transparent brown glass. Wrinkled indicates a wrinkled texture observed along the inclusion–host interface. Devitrified indicates speckled devitrification of the glass.
Crystals: Indicates the presence of microlites inside the inclusion. Qualitative energy dispersive analysis by electron microprobe shows that the microlites are plagioclase. Large indicates crystals greater than 5 μm.
[a] Cr-spinel crystals present inside the inclusion.

Table 2
FTIR data for H_2O in melt inclusions from Xitle volcano

Sample	Thickness	Total H_2O (3530 cm^{-1})		OH (4500 cm^{-1})		Molecular H_2O (5200 cm^{-1})		Molecular H_2O (1630 cm^{-1})	
	(μm)	Absorbance	H_2O (wt.%)	Absorbance	H_2O (wt.%)	Absorbance	H_2O (wt.%)	Absorbance	H_2O (wt.%)
Layer 1									
X1-2	90	0.3310	0.38	–	–	–	–	0.0060	0.01
X1-4	90	0.2390	0.27	0.0036	0.30	–	–	0.0113	0.02
X1-5	60	0.3288	0.56	0.0033	0.41	0.0007	0.08	0.0054	0.01
X1-7	68	0.2758	0.42	0.0032	0.36	0.0015	0.14	0.0182	0.04
X1-8	60	0.2365	0.40	0.0030	0.38	0.0001	0.01	0.0068	0.02
X1-9	32	0.0945	0.30	0.0010	0.23	0.0004	0.07	0.0047	0.02
X1-10	55	0.3221	0.60	0.0032	0.44	–	–	0.0022	0.01
X1-11	65	0.2039	0.32	0.0015	0.17	–	–	0.0127	0.03
X1-12	90	0.1899	0.22	0.0006	0.05	–	–	0.0127	0.02
X1-13	100	0.1927	0.20	0.0015	0.11	–	–	0.0014	0.00
X1-14	65	0.2232	0.35	0.0019	0.23	0.0006	0.06	0.0279	0.07
X1-15	38	0.0564	0.15	0.0000	0.00	0.0007	0.07	0.0041	0.02
Layer 2									
X2-1	75	0.2050	0.28	0.0027	0.28	0.0007	0.06	–	–
X2-2	91	0.1981	0.22	0.0022	0.19	–	–	0.0093	0.02
X2-4	175	2.2400	1.30	0.0194	0.84	0.0067	0.25	0.2958	0.27
X2-5	90	0.2608	0.30	0.0045	0.38	–	–	0.0102	0.02
X2-6	100	0.2378	0.24	–	–	–	–	0.0069	0.01
X2-7	60	0.1658	0.28	0.0020	0.25	–	–	0.0100	0.03
X2-8	88	0.2531	0.30	0.0012	0.11	0.0013	0.10	0.0110	0.02
X2-9	68	0.1270	0.19	0.0016	0.18	–	–	0.0037	0.01
X2-10	135	0.4354	0.33	0.0035	0.20	–	–	0.0326	0.04
X2-11	95	0.2661	0.44	0.0020	0.32	0.0007	0.05	0.0365	0.09
X2-12	58	0.1274	0.22	0.0009	0.12	0.0005	0.06	0.0064	0.02
X2-14	42	0.1217	0.29	–	–	–	–	0.0048	0.02
X2-17	82	0.2605	0.32	0.0015	0.14	0.0005	0.04	0.0111	0.02
X2-18	62	0.1142	0.19	0.0010	0.12	–	–	0.0083	0.02
X2-19	50	0.0486	0.10	0.0009	0.14	0.0009	0.12	0.0025	0.01
X2-20	30	0.0767	0.26	0.0000	0.00	0.0006	0.13	–	–
X2-21	52	0.1064	0.20	0.0014	0.19	0.0009	0.10	0.0056	0.02
Layer 3									
X3-1	80	0.1480	0.19	0.0014	0.13	0.0009	0.07	0.0114	0.02
X3-2	68	0.1682	0.25	0.0015	0.17	0.0010	0.10	0.0163	0.04
X3-3	30	0.2790	0.95	0.0029	0.72	0.0015	0.32	0.0463	0.25
X3-4	50	0.3773	0.81	0.0041	0.62	0.0007	0.09	0.0332	0.11
X3-5	80	0.3250	0.41	0.0030	0.28	0.0009	0.07	0.0311	0.06
X3-6	45	0.1132	0.26	–	–	–	–	0.0114	0.04
X3-8	105	0.7295	0.71	0.0066	0.48	0.0025	0.15	0.0740	0.11
X3-9	42	0.3425	0.85	0.0042	0.66	0.0018	0.28	0.0390	0.15

Absorbance intensities for total water (3530 cm^{-1}), hydroxyl (OH; 4500 cm^{-1}), and molecular H_2O (5200 cm^{-1} and 1630 cm^{-1}) were determined by infrared spectroscopy as described in the text. Inclusion thicknesses were measured using a microscope with a calibrated eyepiece. Water concentrations expressed as wt.% H_2O were calculated using absorption coefficients from Dobson et al. (unpublished data, cited in Dixon et al., 1995) and Dixon et al. (1995). A room temperature glass density of 2800 kg/m^3 was assumed for all inclusions. Based on multiple analyses of individual inclusions, the precision of the spectroscopic measurement for the 3530 cm^{-1} band is ~10% (relative), except for the very-low-water-content inclusions, for which it is ±0.01 to ±0.02 wt% (absolute). Accuracies are limited by uncertainties in molar absorption coefficients and in the background correction procedures, and have been estimated to be ~10% for the measurement of total H_2O (Dixon et al., 1995).
– denotes values below detection.

Table 3
FTIR data for carbonate in melt inclusions from Xitle volcano

Sample	Thickness	CO_3^{2-} (1430 and 1515 cm^{-1})	
	(μm)	Absorbance	CO_2 (ppm)
Layer 2			
X2-4	175	0.1030	348
Layer 3			
X3-3	30	0.018	354

Absorbance intensities for carbonate (1515 and 1430 cm^{-1}) were determined by FTIR. Carbonate contents were calculated as ppm CO_2 using absorption coefficients from Dixon and Pan (1995).
The average precision for absorbances of the 1515 and 1430 cm^{-1} bands is ±30%, mainly due to uncertainties in the subtraction and background fitting procedure.

cm^{-1} band (molecular H_2O). The absorption coefficient for the 3530 cm^{-1} band is not strongly dependent on composition (Ihinger et al., 1994), and our total H_2O (3530 cm^{-1}) values show good agreement with total H_2O calculated from the sum of the water species bands (4500 cm^{-1} and either 5200 cm^{-1} or 1630 cm^{-1}).

4.3. Electron microprobe analysis

We measured the major and minor element compositions of melt inclusions, matrix glasses, and olivine host crystals using a Cameca SX50 electron microprobe with four wavelength dispersive spectrometers in the Department of Geology and Geophysics at Texas A&M University (Tables 4 and 5). Standards included a combination of natural glasses and minerals. The conditions selected for analyses of glass inclusions and matrix glasses were 10 nA beam current, an electron gun voltage of 15 kV, and 10 μm beam diameter. Sulfur was analyzed using an anhydrite standard, 60 s on-peak counting time, and a S K_α wavelength offset measured on pyrite, which corresponds approximately to the $S^{6+}/\Sigma S$ ratio expected for a basaltic glass equilibrated at the FMQ oxygen buffer (Wallace and Carmichael, 1994). This oxidation state is appropriate based on whole rock $Fe^{3+}/\Sigma Fe$ for a Xitle basalt (Wallace and Carmichael, 1999). Analyses of glass standard VG-2 using this procedure yielded a S concentration of 0.137 ± 0.006 ($n = 11$), similar to the values reported by Dixon et al. (1991) and Dixon and Clague (2001). For analyzing the olivine host crystals, instrumental conditions were 10 nA beam current, voltage of 15 kV, and beam diameter of 1 μm.

5. Results

5.1. Melt inclusion textures

Melt inclusions were closely inspected during sample preparation as an aid to understanding the processes of inclusion formation and to identify features indicative of syneruptive volatile loss (Table 1). Most melt inclusions in olivine have irregular subangular to subrounded shapes but some inclusions are elliptical (Fig. 2). We distinguish three main types of inclusions: (1) glass that is fully enclosed within a crystal (termed glass or melt inclusions; Fig. 2A–C); (2) glass that is connected to the rim of the crystal by a thin neck (termed hourglass inclusions by Anderson, 1991); and (3) glass in open reentrants (commonly called embayments; Fig. 2D). These different textural types reflect decreasing degrees of isolation from the coexisting melt at the time of eruptive quenching. After entrapment, enclosed melt inclusions can only communicate with the external coexisting melt by diffusion through the host crystal. Hourglass inclusions are in physical continuity with the coexisting external melt, and they may communicate with it by diffusion through the melt in the neck. In addition, gas bubbles in bubble-bearing hourglass inclusions may expand, depleting the melt in dissolved volatiles as melt is expelled through the neck (Anderson, 1991). Bubble-free hourglass inclusions, however, can change their volatile contents only by diffusion; their volatile concentrations therefore reflect the volatiles dissolved in the coexisting external melt near the time of the eruption. Reentrant glass will also communicate with the coexisting ambient magma by diffusion through the melt. Large reentrants that lack vapor bubble(s) (Fig. 2D) can also be used to measure the volatiles dissolved in the coexisting external melt shortly before eruption.

Table 4
Major element compositions of melt inclusions from Xitle volcano

Inclusion	X1-2	X1-4	X1-7	X1-8	X1-9	X1-10	X1-11	X1-12	X1-13	X1-14	X1-15	X2-1	X2-2	X2-4	X2-5	X2-6	X2-9	X2-11	X2-12	X2-17	X2-19	X2-20	X2-21	X3-1	X3-3	X3-4	X3-6	X3-8	X3-9
SiO_2	55.0	55.6	56.4	54.8	55.9	55.9	56.8	57.0	56.2	55.7	58.0	55.4	55.0	52.0	56.3	55.6	54.9	54.9	55.8	55.2	56.7	55.1	56.0	55.1	59.0	60.3	56.5	58.7	58.0
TiO_2	2.65	2.69	3.12	2.31	2.76	2.78	3.08	3.09	2.86	2.78	2.71	2.60	2.78	1.93	2.87	2.64	2.49	2.57	2.60	2.41	2.88	2.70	3.06	3.01	2.21	2.31	1.94	2.1	1.84
Al_2O_3	15.0	15.2	15.2	15.7	15.0	15.0	15.1	14.9	14.6	14.9	15.0	15.1	14.6	17.0	14.7	15.0	14.8	14.7	15.3	15.2	14.6	15.3	14.5	14.7	15.5	15.9	17.1	15.2	16.8
FeO^T	8.84	7.45	7.57	8.51	8.13	8.64	8.00	8.23	8.24	8.82	8.19	8.75	7.60	7.09	8.08	8.76	9.24	8.82	8.48	8.51	8.91	8.98	9.04	9.32	6.86	5.98	6.79	6.87	6.4
MnO	0.16	0.15	0.12	0.16	0.12	0.16	0.14	0.16	0.16	0.16	0.15	0.14	0.12	0.11	0.14	0.16	0.15	0.16	0.13	0.16	0.16	0.16	0.16	0.16	0.11	0.11	0.12	0.14	0.13
MgO	4.29	4.14	3.85	4.33	4.08	3.97	3.74	3.67	3.66	3.93	3.63	4.12	3.88	5.03	3.80	4.09	4.19	4.13	4.12	4.13	3.66	4.04	3.80	3.9	2.8	2.84	3.06	2.87	3.02
CaO	7.93	7.55	6.81	7.88	7.65	7.31	6.84	6.84	6.89	7.28	6.40	7.56	7.75	8.31	7.19	7.54	7.53	7.65	7.48	7.55	6.73	7.33	6.97	7.24	5.61	5.4	6.71	5.68	6.52
Na_2O	4.15	4.39	4.10	4.15	4.03	3.97	4.10	4.42	4.14	3.82	3.87	3.95	4.12	4.01	4.23	4.22	3.90	3.69	3.97	4.03	3.69	3.96	3.79	3.83	4.35	4.64	4.59	4.54	4.57
K_2O	1.79	2.04	2.24	1.78	1.96	2.04	2.28	2.30	2.20	1.99	2.39	1.94	2.04	1.32	2.32	1.95	1.85	1.93	1.97	1.75	2.31	1.93	2.16	2.12	2.12	2.33	2.19	2.15	2.13
P_2O_5	0.87	0.98	1.13	0.76	0.95	0.92	1.07	1.08	1.14	1.02	1.16	0.94	1.12	0.75	1.07	0.91	0.93	1.01	0.95	0.93	1.12	0.94	1.11	0.96	0.64	0.67	0.49	0.61	0.54
S	b.d.	b.d.	0.007	0.010	b.d.	0.005	0.011	b.d.	0.014	0.006	0.013	0.012	b.d.	0.097	b.d.	0.018	0.006	0.013	0.010	0.013	0.010	0.010	0.011	b.d.	b.d.	b.d.	0.031	0.014	0.036
H_2O	0.38	0.27	0.42	0.40	0.30	0.60	0.32	0.22	0.20	0.35	0.15	0.28	0.22	1.30	0.30	0.24	0.19	0.44	0.22	0.32	0.10	0.26	0.20	0.19	0.95	0.81	0.26	0.71	0.85
CO_2	b.d.	b.d.	b.d.	b.d.	b.d.	b.d.	b.d.	b.d.	b.d.	b.d.	b.d.	b.d.	b.d.	348	b.d.	b.d.	b.d.	b.d.	b.d.	b.d.	b.d.	b.d.	b.d.	b.d.	354	b.d.	b.d.	b.d.	b.d.
Total	101.0	100.5	100.9	100.8	100.9	101.3	101.5	101.9	100.3	100.8	101.7	100.8	99.2	99.0	101.0	101.1	100.1	100.0	101.0	100.2	100.9	100.7	100.8	100.6	100.1	101.3	99.8	99.5	100.7
Olivine Fo%	84.8	86.2	84.0	85.2	84.4	84.8	85.1	84.7	85.2	84.3	84.5	84.0	84.5	85.0	83.7	85.7	84.1	84.4	84.9	84.4	84.7	84.7	83.8	83.9	85.9	86.1	85.2	86.1	86.0
Glass Mg#	0.52	0.55	0.53	0.53	0.53	0.51	0.51	0.50	0.50	0.50	0.50	0.51	0.53	0.61	0.51	0.51	0.50	0.51	0.52	0.52	0.48	0.50	0.48	0.48	0.48	0.51	0.50	0.48	0.51
Compositions corrected for post-entrapment crystallization																													
SiO_2	53.0	54.0	52.9	53.0	54.2	53.5	54.4	54.2	54.1	53.6	55.3	53.6	54.2	52.2	54.5	53.2	53.3	53.4	53.7	53.7	54.1	53.1	53.8	53.0	56.7	57.8	54.9	56.6	56.0
TiO_2	2.37	2.45	2.37	2.07	2.52	2.46	2.75	2.72	2.53	2.47	2.41	2.36	2.59	1.90	2.62	2.32	2.25	2.33	2.33	2.19	2.51	2.40	2.72	2.65	1.96	2.09	1.76	1.85	1.66
Al_2O_3	13.4	13.8	13.4	14.1	13.7	13.3	13.4	13.1	12.9	13.2	13.4	13.7	13.6	16.7	13.4	13.2	13.4	13.3	13.7	13.9	12.7	13.6	12.9	13.0	13.7	14.3	15.5	13.4	15.1
FeO^T	9.63	8.19	9.63	9.29	8.83	9.54	8.86	9.15	9.34	9.79	9.08	9.54	8.44	7.43	8.83	9.69	10.15	9.73	9.30	9.33	10.06	9.92	10.05	10.39	8.15	6.90	7.87	8.24	7.32
MnO	0.14	0.14	0.14	0.14	0.11	0.14	0.12	0.14	0.14	0.14	0.13	0.13	0.11	0.11	0.13	0.14	0.14	0.15	0.12	0.15	0.14	0.14	0.14	0.14	0.10	0.10	0.11	0.12	0.11
MgO	7.91	7.56	7.91	8.01	7.02	7.94	7.39	7.65	8.07	7.89	7.25	7.37	6.92	6.25	6.71	8.45	7.79	7.77	7.77	7.43	8.32	8.00	7.72	8.17	7.26	6.27	6.85	7.75	6.62
CaO	7.10	6.87	7.10	7.08	7.00	6.47	6.10	6.01	6.09	6.47	5.69	6.86	7.21	8.16	6.57	6.61	6.80	6.92	6.70	6.89	5.86	6.52	6.19	6.38	4.97	4.88	6.09	5.01	5.88
Na_2O	3.72	3.99	3.71	3.73	3.69	3.51	3.65	3.88	3.66	3.40	3.44	3.58	3.83	3.94	3.86	3.70	3.52	3.34	3.56	3.67	3.21	3.52	3.37	3.38	3.86	4.19	4.16	4.01	4.12
K_2O	1.60	1.86	1.60	1.60	1.79	1.80	2.03	2.02	1.94	1.77	2.13	1.76	1.90	1.30	2.12	1.71	1.67	1.75	1.76	1.60	2.01	1.72	1.92	1.87	1.88	2.10	1.99	1.90	1.92
P_2O_5	0.78	0.89	0.78	0.68	0.87	0.81	0.95	0.95	1.01	0.91	1.03	0.85	1.04	0.74	0.98	0.80	0.84	0.91	0.85	0.85	0.97	0.84	0.99	0.85	0.57	0.60	0.45	0.54	0.49
S	b.d.	b.d.	0.006	0.009	b.d.	0.004	0.010	b.d.	0.012	0.005	0.012	0.011	b.d.	0.084	b.d.	0.016	0.005	0.012	0.009	0.012	0.008	0.009	0.010	b.d.	b.d.	b.d.	0.028	0.012	0.032
H_2O	0.34	0.25	0.39	0.36	0.27	0.53	0.29	0.19	0.17	0.31	0.14	0.25	0.20	1.27	0.27	0.21	0.17	0.40	0.20	0.29	0.09	0.23	0.18	0.17	0.84	0.74	0.23	0.62	0.76
CO_2	b.d.	b.d.	b.d.	b.d.	b.d.	b.d.	b.d.	b.d.	b.d.	b.d.	b.d.	b.d.	b.d.	338	b.d.	b.d.	b.d.	b.d.	b.d.	b.d.	b.d.	b.d.	b.d.	b.d.	312	b.d.	b.d.	b.d.	b.d.
Total	100.00	100.00	100.00	100.00	100.00	100.00	100.00	100.00	100.00	100.00	100.00	100.00	100.00	100.00	100.00	100.00	100.00	100.00	100.00	100.00	100.00	100.00	100.00	100.00	100.00	100.00	100.00	100.00	100.00
Mg#	0.65	0.67	0.65	0.66	0.64	0.65	0.65	0.65	0.66	0.64	0.64	0.63	0.65	0.65	0.63	0.66	0.63	0.64	0.65	0.64	0.65	0.64	0.63	0.64	0.66	0.67	0.66	0.68	0.67
%PEC	10	9	7	10	8	11	10	11	12	11	10	9	8	3	8	12	10	10	10	9	13	11	11	12	12	9	10	13	10
P sat. (bar)	12	7	16	14	8	30	9	4	3	10	2	7	4	891	8	5	3	17	4	9	1	6	3	3	741	59	6	41	62

Major element compositions by electron microprobe. Total iron is reported as FeO. H_2O and CO_2 are by FTIR (see Tables 2 and 3). All analyses in wt.% except for CO_2 in ppm.

Mg# is calculated as $Mg^{2+}/Mg^{2+}+Fe^{2+}$ assuming that 80% of the total iron is present as Fe^{2+}.

%PEC is the amount of post-entrapment crystallization determined as described in the text.

P sat. is the vapor saturation pressure in bars calculated using experimental solubility data (Dixon et al., 1995).

Of the analyzed melt inclusions, seven of 20 fully enclosed inclusions contain vapor bubbles, three of seven hourglass inclusions contain vapor bubbles, and six of 10 reentrants contain bubbles (Table 1). For each of these three inclusion types, the range and median volume % of the inclusion occupied by the vapor bubble (calculated from petrographic observations) are as follows: enclosed, 2–10 vol.%, median 3 vol.%; hourglass, 1–4 vol.%, median 2 vol.%; reentrant, 0.1–3 vol.%, median 2 vol.%. The relatively small sizes of most bubbles in enclosed inclusions suggest that they formed after entrapment because of differential shrinkage of melt and the crystal host during cooling (Roedder, 1984; Lowenstern, 1995). However, the largest bubbles could be primary, or in the case of hourglass inclusions and reentrants, may result from decompression during eruption (Anderson, 1991).

Most of the analyzed melt inclusions contain microlites (Table 1). In many cases, the microlites are dispersed throughout the interior of the inclusion and do not appear to have nucleated and grown from the inclusion walls. Another textural feature observed for many inclusions is that the inclusion–host interface appears wrinkled. This texture is somewhat similar to textures seen in inclusions that have been experimentally reheated (Wallace, unpublished data), suggesting that the wrinkling is a result of rapid dissolution. This texture may form in natural inclusions due to reheating, perhaps as a result of magma mixing.

5.2. Post-entrapment crystallization of olivine in melt inclusions

Forsterite contents of olivine phenocrysts from Xitle tephra range from $Fo_{83.7}$ to $Fo_{86.2}$ (average $Fo_{84.5}$) indicating crystallization from relatively MgO-rich melts. The high forsterite contents of the olivines contrast with the low Mg# of the melt inclusions (0.48–0.61; see Table 4). To account for the compositional effects of post-entrapment crystallization of olivine along the inclusion walls, we have added 1% increments of equilibrium olivine, calculated using Fe–Mg partitioning (Roedder and Emslie, 1970), to the composition of each inclusion until it is in equilibrium with the olivine host (Table 4). Most melt inclusions require less than 15% olivine addition to restore equilibrium with the olivine host. Relative to analyzed compositions, restored melt inclusion compositions have higher MgO (by as much as a factor of 2.5) and FeO^T ($<15\%$ increase) and have about 2 wt.% lower SiO_2. The similarity of whole rock FeO values to FeO in many restored inclu-

Table 5
Major element compositions of matrix glass samples from Xitle volcano

Inclusion	1-A	1-B	1-C	2-A	2-B	2-C	3-A	3-B	3-C	Unit IV
SiO_2	55.02	54.90	55.24	54.63	55.26	55.20	59.58	58.72	59.66	52.32
TiO_2	2.20	2.77	2.76	2.65	2.23	2.65	2.16	1.96	2.14	2.53
Al_2O_3	16.00	14.40	14.64	14.25	16.52	14.58	14.92	16.61	14.96	15.02
FeO^T	8.36	9.41	9.33	9.60	8.04	9.04	7.67	6.79	7.64	9.54
MnO	0.16	0.15	0.16	0.12	0.16	0.16	0.13	0.14	0.13	0.19
MgO	3.72	4.07	3.76	4.20	3.74	4.33	2.82	2.57	3.12	4.92
CaO	7.66	7.01	7.24	7.16	7.83	7.36	5.42	6.29	5.54	8.58
Na_2O	4.09	4.06	4.01	3.94	4.14	4.05	4.57	4.70	4.58	4.31
K_2O	1.84	1.97	1.98	2.01	1.63	1.84	2.20	1.91	2.16	1.55
P_2O_5	0.81	0.98	1.00	0.97	0.83	0.90	0.62	0.58	0.64	0.68
S	0.008	0.004	0.005	0.009	0.004	0.010	0.015	0.008	0.006	0.008
Total	99.86	99.72	100.14	99.54	100.38	100.11	100.11	100.26	100.57	99.65
Glass Mg#	0.50	0.49	0.47	0.49	0.51	0.52	0.45	0.46	0.48	0.53

Matrix glass samples are from layer 1 (1-A, 1-B, 1-C), layer 2 (2-A, 2-B, 2-C), and layer 3 (3-A, 3-B, 3-C). Pillow rim glass is from lava flow unit IV.
Major element compositions by electron microprobe. Total iron is reported as FeO. All analyses in wt.%.
Mg# is calculated as $Mg^{2+}/Mg^{2+}+Fe^{2+}$ using the analyzed composition of the matrix glass and assuming that 80% of the total iron is present as Fe^{2+}.

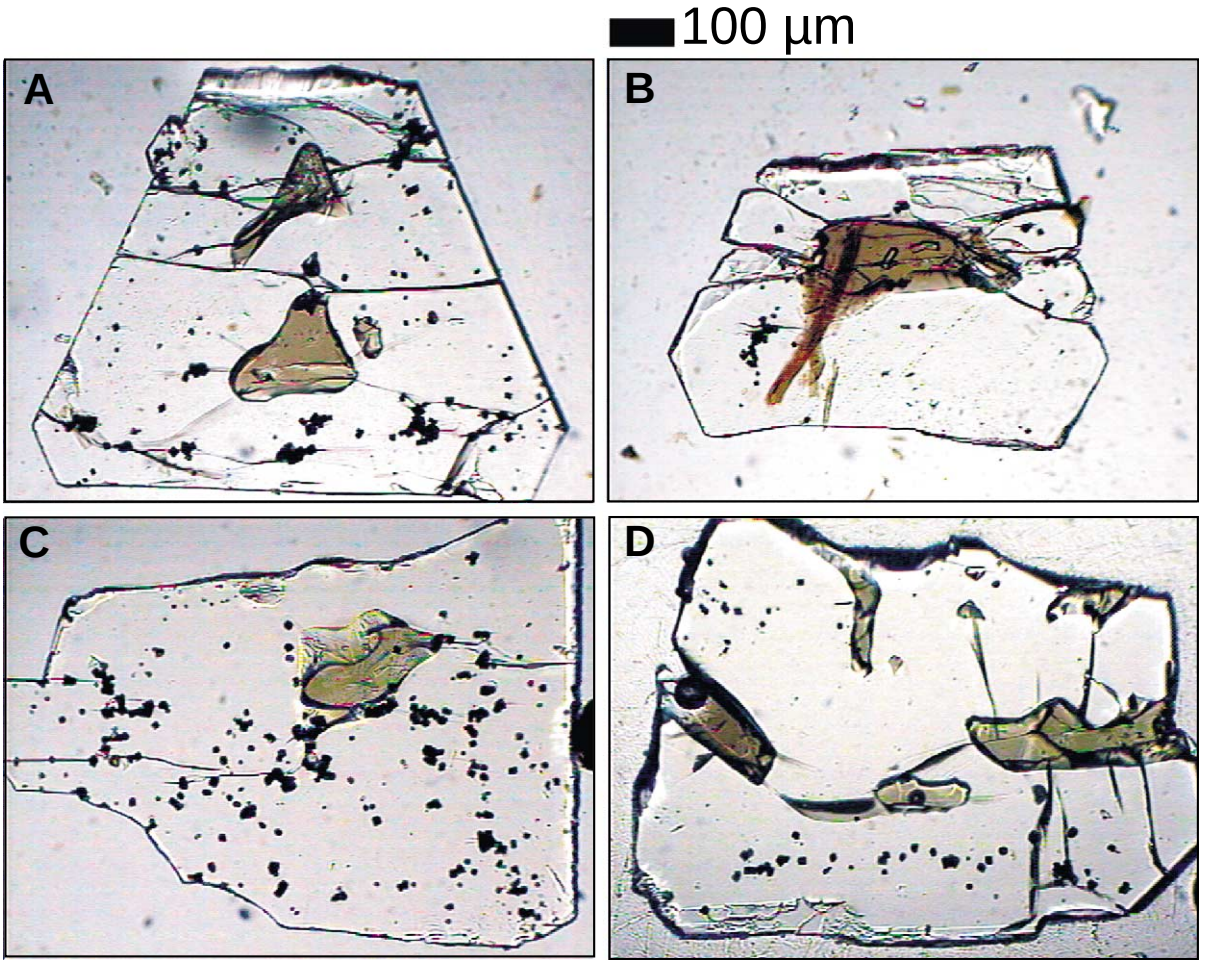

Fig. 2. Photomicrographs of melt inclusion-bearing olivine crystals from Xitle volcano after sectioning for infrared spectroscopy. (A) Inclusion X1-8 (fully enclosed) shows the irregular form that is very common for Xitle melt inclusions. (B) Fully enclosed inclusion X1-7. Two relatively large plagioclase microlites are present inside the inclusion. Microlites such as these (>5 µm) were considered 'large' in Table 1. (C) Fully enclosed inclusion X2-12, also showing irregular shape. (D) Crystal X2-13 showing three reentrant inclusions. Note that the reentrant at left contains a vapor bubble whereas the large reentrant at right is bubble-free.

sion compositions suggests post-entrapment olivine growth by fractional rather than equilibrium crystallization (T. Sisson, written communication), and thus provides some validation for the recalculation procedure that we have used.

5.3. *Major element compositions of melt inclusions and matrix glasses*

The major element compositions of melt inclusions after correction for post-entrapment olivine crystallization have SiO_2 contents that range from 52 to 58 wt.%, with most values between 53 and 55 wt.% SiO_2. In the total alkalies vs. silica diagram (Fig. 3) the inclusions are transitional between the alkaline and subalkaline fields. A group of Xitle melt inclusions from the first explosive event (tephra layer 3) are distinct from those of the other tephra layers in having higher SiO_2 contents (55–58 wt.%) and plotting clearly in the subalkaline field. For each of the tephra layers, matrix glass compositions are similar to but slightly more evolved than those of associated melt inclusions. This indicates that additional

crystallization of the magmas continued after the melt inclusions, reentrants and hourglasses were trapped.

Whole rock samples from Xitle lava flows have lower SiO_2 and incompatible element concentrations (K_2O, TiO_2, P_2O_5) than melt inclusions. However, the whole rock compositions lie along the linear trends for melt inclusions and matrix glasses from tephra layers 1 and 2 (Fig. 4) and have similar incompatible element ratios. This is the pattern that would be expected for a comagmatic relationship between magma (whole rock analyses) and associated olivine phenocrysts, included melts, and residual melt (matrix glass). These relations demonstrate that the olivines are not xenocrystic and that they probably crystallized from the host magma in which they were erupted. We note, however, that no analyzed whole rock samples have compositions that lie at the less differentiated end of the melt inclusion compositions from tephra layer 3. Layer 3 matrix glass samples have similarly low TiO_2 and P_2O_5 to the inclusions indicating that the layer 3 olivines are not xenocrystic (Figs. 3 and 4). Because all major flow units from Xitle have been analyzed (Cervantes and Molinero, 1995; Wallace and Carmichael, 1999), this observation indicates that no Xitle lava flows have compositional similarities to layer 3 tephra.

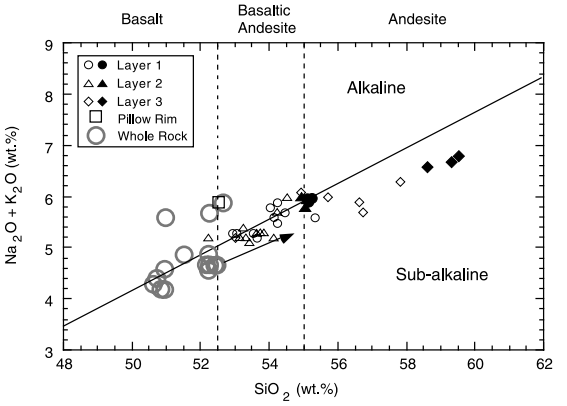

Fig. 3. Diagram showing SiO_2 vs. total alkalis (Na_2O+K_2O) in melt inclusion glasses, matrix glasses, and whole rock samples from Xitle volcano. Melt inclusion compositions corrected for post-entrapment crystallization of olivine are shown as open symbols, matrix glass compositions as solid symbols, and whole rock analyses as large open gray circles. All analyses of matrix and melt inclusion glasses have been normalized to sum to 100% on an anhydrous basis with all iron as FeO. Whole rock analyses are from Cervantes and Molinero (1995) and Wallace and Carmichael (1999). The composition of pillow rim glass from a portion of lava flow unit V that flowed into a shallow lake is shown as an open square. Dashed lines show the limits between basalt and basaltic-andesite (52.5 wt.% SiO_2) and between basaltic-andesite and andesite (55 wt.% SiO_2). Shown for reference is the dividing line separating alkali olivine basalts and subalkaline basalts (tholeiites) in Hawaii (Macdonald and Katsura, 1964). The effect on melt composition of 10 wt.% olivine crystallization is shown as an arrow.

5.4. H_2O, CO_2, and S in melt inclusions

Analyzed H_2O, CO_2 and S concentrations have been corrected for the effects of post-entrapment growth of olivine as described above (Table 4). These corrected values will be used throughout subsequent figures and discussion. Dissolved H_2O concentrations in melt inclusions from tephra layer 3 (first explosive phase) are slightly higher, on average, than those in layers 1 and 2 (Fig. 5). Average values ($\pm 1\sigma$) for fully enclosed inclusions are 0.64 ± 0.24 wt.% H_2O (layer 3), 0.39 ± 0.36 wt.% (layer 2), and 0.36 ± 0.11 wt.% (layer 1). For inclusions from a given tephra layer, H_2O contents of fully enclosed inclusions, hourglasses, and reentrants overlap (Fig. 5), but on average, fully enclosed inclusions have higher values. In addition, abundant microlites are more common in reentrants and hourglasses than in fully enclosed inclusions (Fig. 5).

H_2O behaves as an incompatible element during crystallization of basaltic melt. Because matrix glass compositions are more evolved than the melt inclusions, the H_2O concentrations of the matrix melt just before eruption would have been greater than the values of the inclusions. Using the H_2O/K_2O ratios of the two inclusions with the highest H_2O (X2-4, X3-3) and the average K_2O of the matrix glasses from each tephra layer, we estimate that before eruption, the H_2O contents of the melts represented by the different tephra layers were 1.9 wt.% (layer 1), 1.8 wt.% (layer 2) and 0.9 wt.% H_2O (layer 3).

The concentration of dissolved molecular H_2O (5200 cm^{-1}) is below detection in many inclusions. However, in inclusions with more than

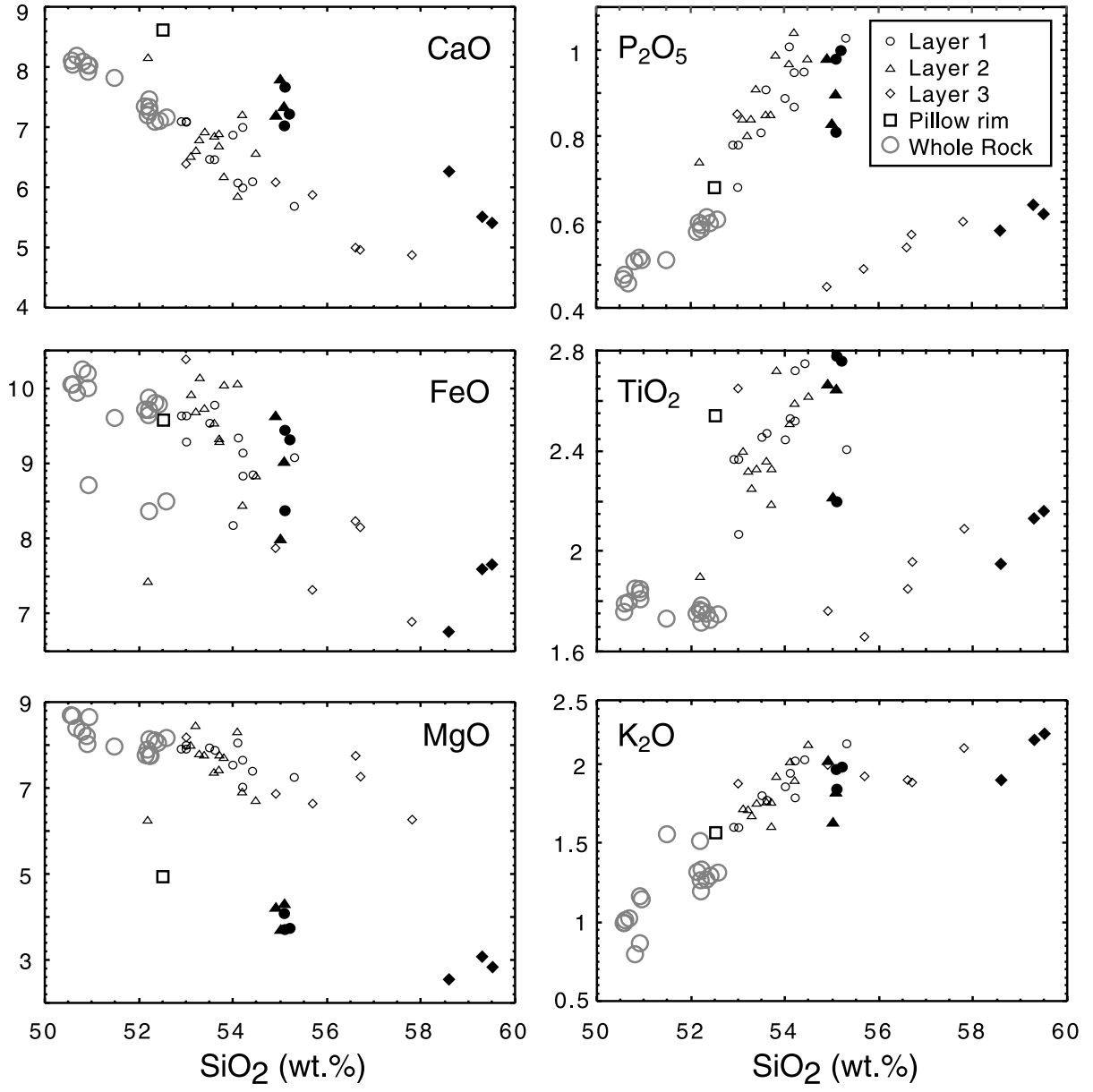

Fig. 4. Major element variation diagrams for melt inclusions, matrix glasses, and whole rock samples from Xitle volcano. Symbols and data sources are given in Fig. 3.

~0.4 wt.% total H_2O, dissolved molecular H_2O varies from 0.06 to 0.32 wt.%. All Xitle inclusions plot near the experimental high-temperature water speciation curve for basaltic melts (Fig. 6), indicating that the dissolved water concentrations are primary and not the result of secondary (low-temperature) hydration of melt inclusion glasses.

Only two of the analyzed inclusions contain measurable CO_2, one from layer 2 (inclusion X2-4, 338 ppm) and the other from layer 3 (inclusion X3-3, 312 ppm) (Table 3). All other inclusions must have CO_2 below the detection limit, which is ~30 ppm for samples with the typical thickness of our sectioned Xitle inclusions.

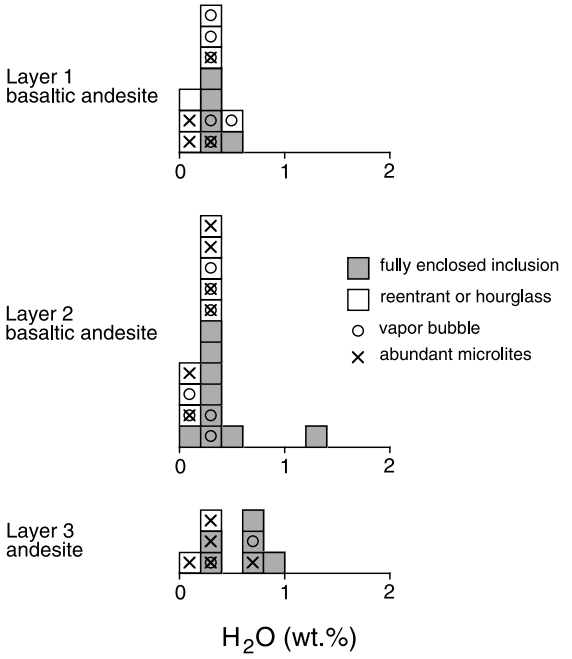

Fig. 5. Histograms showing concentrations of total dissolved H_2O in melt inclusions from Xitle after correction for post-entrapment crystallization (Table 4). Fully enclosed inclusions are denoted by gray shading, whereas reentrant and hourglass inclusions are white; inclusions that contain a vapor bubble are denoted by a circle; inclusions that contain abundant microlites are denoted by an X.

Sulfur concentrations vary from below detection ($\sim$50 ppm) to 1000 ppm but are mostly $\leq$200 ppm (Fig. 7). In general, there is little correlation between H_2O and S, but the three inclusions with highest S contents all have $\geq$0.5 wt.% total H_2O.

6. Discussion

6.1. Pressures of crystallization and melt inclusion formation

The dissolved H_2O and CO_2 concentrations of the melt inclusions are shown in Fig. 8 together with H_2O-CO_2 vapor saturation curves for basaltic melts at pressures of 100–1000 bar and a temperature of 1200°C. If the trapped melts that were quenched to form the glass inclusions were vapor saturated during crystallization of olivine and entrapment of inclusions, then the dissolved H_2O and CO_2 contents can be used to calculate the crystallization pressure (Table 4). If the melts were not vapor saturated, then the H_2O and CO_2 data provide a minimum pressure of crystallization; however, because of the very low solubility of CO_2 in silicate melts, basaltic melts will probably be vapor saturated at crustal pressures (e.g., Roedder, 1984; Dixon and Stolper, 1995). When using dissolved H_2O and CO_2 contents to infer vapor saturation pressures, a complication arises because many melt inclusions contain a

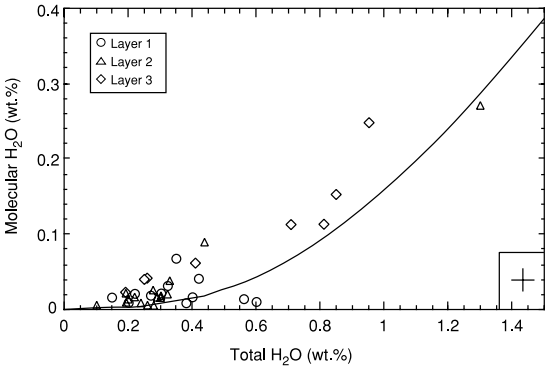

Fig. 6. Total H_2O (3530 cm^{-1}) vs. molecular H_2O (1630 cm^{-1}) in melt inclusions from Xitle volcano (Table 2). The average analytical uncertainty for the measurements is shown in the lower right. Shown for comparison (solid line) is the experimentally determined high-temperature speciation curve for water in tholeiitic melts (Dixon et al., 1995).

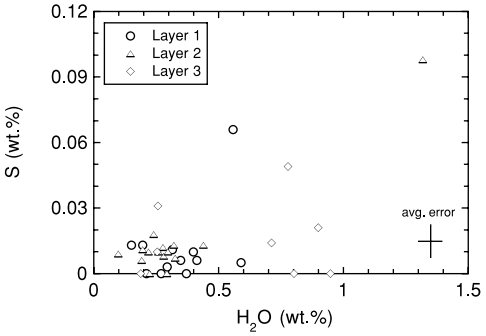

Fig. 7. Plot of total H_2O (wt.%) vs. S (wt.%) in melt inclusions from Xitle volcano. Total H_2O was measured by FTIR using the absorbance of the 3530 cm^{-1} band (Table 2). S contents were measured by electron microprobe (Table 4). The lower limit of detection for S on the microprobe is $\sim$50 ppm. The average analytical uncertainty for the measurements is shown in the lower right.

small vapor bubble that formed during post-entrapment cooling due to the greater thermal expansion of melt relative to the olivine host (Roedder, 1965; Lowenstern, 1995). A significant amount of the CO_2 originally dissolved in the melt is lost to this vapor bubble as it forms (Anderson and Brown, 1993). As a result, vapor saturation pressures based on analyzed dissolved H_2O and CO_2 in the melt (glass) can underestimate the original trapping pressure.

Melt inclusions that are fully enclosed in the olivine host and do not contain vapor bubbles (Table 1) are the most straightforward for estimating entrapment pressure. For all but one of these inclusions (X3-3), the dissolved H_2O concentrations and absence of measurable CO_2 indicate pressures ≤ 100 bar. Similarly, for fully enclosed inclusions that contain vapor bubbles, dissolved CO_2 was also below detection in all but one inclusion (X2-4). The absence of dissolved CO_2 indicates that the composition of the vapor phase formed by melt shrinkage during cooling would have been H_2O-rich and CO_2-poor. Given the high solubility of H_2O in basaltic melt and the relatively small size of the vapor bubbles, the original entrapment pressure of these inclusions, calculated by assuming all vapor in the bubble was originally dissolved in the melt, are only slightly higher than the pressure estimated from the analyzed H_2O content. Only if the vapor phase was relatively CO_2-rich would the original entrapment pressure be significantly higher than the apparent pressure based on measured volatile concentrations (see Anderson and Brown, 1993). Therefore the vapor saturation pressures inferred for fully enclosed inclusions that contain vapor bubbles (except X2-4) are also ≤ 100 bar.

Many of the reentrants and hourglass inclusions that we analyzed in Xitle tephra also do not contain vapor bubbles. This indicates that they did not exsolve volatiles during ascent and eruption. Because such inclusions are connected to external melt, they can be used to infer the pressure of the magma a short time before eruption. The vapor saturation pressures of these bubble-free reentrants and hourglass are ≤ 100 bar, similar to enclosed inclusions. The low vapor saturation pressures for fully enclosed inclusions and bubble-free reentrants and hourglasses indicate that most olivine crystallized at very shallow depths beneath the volcano.

Only two Xitle melt inclusions contain measurable CO_2. These inclusions must have formed at much higher pressures; the calculated vapor saturation pressures are 740 bar (tephra layer 3, inclusion X3-3) and 890 bar (layer 2, inclusion X2-4). Both of these appear to be fully enclosed inclusions. These inclusions demonstrate that some olivine phenocrysts formed at much higher pressures.

6.2. Low-pressure degassing

The variable and commonly low values of dissolved H_2O in enclosed melt inclusions (0.2–1.3 wt.% H_2O) and the very low vapor saturation pressures suggest that crystallizing olivine trapped melts that had already undergone degassing at shallow depths beneath the volcano. An alternative hypothesis, that 0.2–1.3 wt.% H_2O represents the primary values for Xitle magmas, is inconsistent with the absence of measurable CO_2 in all but two of the inclusions. CO_2 is much less soluble than H_2O in basaltic melts and would therefore be expected to degas almost entirely before significant H_2O was lost (Dixon and Stolper, 1995). Calculated degassing paths for basaltic melts can easily explain the variable H_2O in Xitle melt inclusions that have lost all dissolved CO_2 (Fig. 8). Similar results have been reported for Parícutin volcano, further west in the TMVB, and at Stromboli volcano in the Aeolian Islands, Italy. At Parícutin, Luhr (2001) found that only two of 26 fully enclosed inclusions in olivine contain measurable CO_2. These two inclusions have $\sim$4 wt.% H_2O, whereas the other inclusions have 1.8–3.8 wt.% H_2O as well as lower Cl and S. At Stromboli, melt inclusions in typical crystal-rich scoria from Strombolian eruptions have very low H_2O (0.12–0.18 wt.%) and CO_2 below detection, whereas melt inclusions in crystal-poor tephra from more energetic explosions have higher H_2O (2.3–2.8 wt.%) and CO_2 (890–1690 ppm; Metrich et al., 2001).

The hypothesis that low H_2O in the Xitle inclusions is caused by diffusive loss of H_2O through

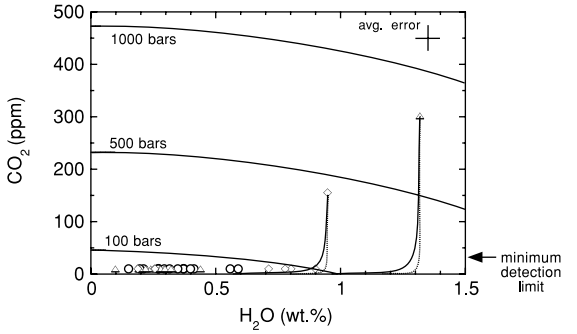

Fig. 8. Plot of total H_2O (wt.%) vs. CO_2 (ppm) for melt inclusions from Xitle volcano (Table 4). Diagonal curves show vapor saturation isobars from 100 to 1000 bars based on experimental solubility measurements and derived thermodynamic models (Dixon et al., 1995). Solid and dashed curves show closed and open system degassing paths, respectively. The paths were calculated using the method of Dixon and Stolper (1995). Minimum detection limit for CO_2 is ~30 ppm. Inclusions below detection are plotted at 10 ppm CO_2 for clarity. The average analytical uncertainty for the measurements is shown in the upper right.

the olivine host can be ruled out. Even though H_2O diffusion could potentially be fast (e.g., Mackwell and Kohlstedt, 1990), diffusion of S and CO_2 through the olivine host should be much slower, yet most inclusions have no CO_2 and have low S contents that are similar to fully degassed basaltic glasses (e.g., Swanson and Fabbi, 1973). Another possibility is that despite our careful petrographic examination before sectioning, the fully enclosed inclusions were able to leak via small cracks in the olivine host or through small melt-filled necks connecting the inclusions to the surface of the host crystal. Because leakage would be caused by the higher pressure of the inclusion relative to its surroundings, this would form vapor bubbles in the inclusions (e.g., Anderson, 1991; Lowenstern, 1995). Most of the enclosed inclusions do not have vapor bubbles (Fig. 5), so leakage as a cause of the low volatile contents seems unlikely. A final possibility is that inclusion volatile contents re-equilibrated by diffusion involving microcracks in the host or melt-filled necks such that no bubble was formed in the inclusion. We consider this unlikely because at the relevant conditions, diffusion of CO_2 is slower than H_2O (possibly by as much as a factor of 10) and S diffusion is about two orders of magnitude slower than H_2O (Watson, 1994). If this type of diffusive leakage was responsible for the low H_2O contents of the inclusions, we would expect more of the inclusions to have high S and measurable CO_2.

We consider it significant that the rare inclusions with measurable CO_2 contain few to no microlites. One interpretation of the presence of microlites and larger crystals in low-H_2O melt inclusions could be that they were formed as the magma was degassing but before the melt was trapped inside growing olivine crystals. Loss of H_2O from melt increases the liquidus temperature, which should result in rapid crystallization (Anderson, 1973; Eichelberger, 1995).

6.3. Controls on explosive vs. effusive eruption at Xitle volcano

The Xitle eruption was dominantly effusive with fluid lava flows accounting for ~95% of the total dense rock erupted material. The paucity of tephra from Xitle contrasts with the eruptive behavior of Parícutin volcano to the west in Michoacán in which tephra deposits account for ~60% of the eruptive products (Fries, 1953). Possible factors that caused this difference are the higher initial water content (~4 wt.%; Luhr, 2001) and greater viscosity of Parícutin magmas due to higher silica contents. However, the H_2O contents of Xitle magmas (≤1.9 wt.% for matrix melt at time of eruption) are more than sufficient to produce high lava fountains or sustained explosive eruptions because fragmentation would occur in the conduit several hundred meters below the surface (Fig. 9; Wilson, 1980; Head and Wilson, 1987; Parfitt and Wilson, 1995). The dominance of effusive lavas at Xitle indicates very efficient degassing of magma before or during extrusion. Unfortunately, we have not been able to analyze any melt inclusions from lava samples because they are crystalline and unsuitable for volatile analysis.

The tephra deposits at Xitle provide important information concerning the processes that govern shallow gas loss from basaltic magmas and control whether eruptions will be explosive or effusive. Melt inclusions in the first erupted tephra

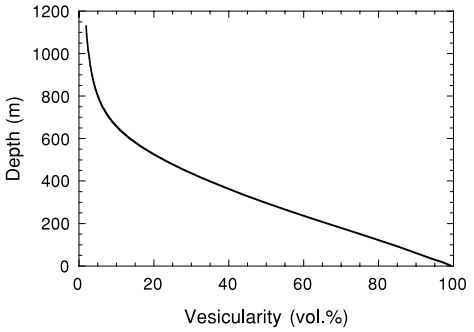

Fig. 9. Depth vs. vesicularity for ascending basaltic magma with an initial H_2O content of 1.3 wt.%. Calculation assumes a lithostatic pressure gradient (Giberti and Wilson, 1990; Parfitt and Wilson, 1995) and uses solubility and degassing relations from Dixon and Stolper (1995). Fragmentation will occur somewhere in the range from 60–90 vol.% vesicles, corresponding to depths <300 m below the surface.

(layer 3) have higher SiO_2, and lower TiO_2 and P_2O_5, than those in the middle (layer 2) and last (layer 1) erupted layers (Fig. 4). Geochemically the layer 3 inclusions are similar to the subduction-related calc-alkaline volcanic rocks that are volumetrically more abundant in the Sierra Chichináutzin volcanic field than are the transitional to alkalic lavas erupted from Xitle (Wallace and Carmichael, 1999; Cervantes, 1999). The stratigraphy at Xitle shows that following an initial, Strombolian, scoria cone-building phase, activity was largely effusive, punctuated briefly by the explosive phase that deposited the tephra from which our melt inclusions are derived. The unusual composition of the melt inclusions and matrix glass in the lowermost tephra layer suggests that the change in the eruptive style was associated with a change in composition from mafic magma to a more viscous andesitic magma that erupted explosively. The distribution of the fall deposits and the lack of soil between the layers indicates that the three ash deposits formed in close succession (Delgado et al., 1998). Although melt inclusions in the first layer are andesitic, those in the subsequent two layers are basaltic andesite, much closer in composition to basaltic magmas that erupted effusively from Xitle (Figs. 3 and 4). The change in composition recorded by the layer 3 tephra somehow interrupted the efficient degassing that allowed effusive eruptions of basalt. It is important to note that this batch of more andesitic magma did not form as a result of crystal fractionation of mafic magma similar to the lavas at Xitle but must instead reflect a magma mixing or recharge event. The evidence for this is that melt inclusions from tephra layer 3 have significantly different P_2O_5 and TiO_2 from melt inclusions from the other layers, as well as different K_2O/TiO_2 and K_2O/P_2O_5 from the whole rock analyses of the mafic lava flows from Xitle (Fig. 4).

In some basaltic eruptions, a switch from effusive back to explosive eruption is the result of influx of ground or surface water such that the eruption becomes phreatomagmatic (Houghton et al., 1999). In the case of Xitle, involvement of external water seems unlikely to be the main factor in causing a new explosive phase because the onset of the explosive phase coincides with a change in magma composition.

The process of non-explosive gas release from silicic magmas has been extensively investigated. Effusive eruptions of silicic magma appear to involve magma with initially high H_2O concentrations (Eichelberger et al., 1986; Newman et al., 1988; Westrich et al., 1988; Martel et al., 1998). That such magmas are erupted non-explosively requires that water be lost through the surrounding country rock prior to extrusion. One possible mechanism by which gas loss may occur is if magma decompression induces sufficient vesicularity to form bubbly magma that is permeable to gas (Eichelberger et al., 1986; Westrich et al., 1988; Eichelberger, 1989, 1995; Westrich and Eichelberger, 1994). In silicic eruptions, Eichelberger et al. (1986) proposed that a funnel-shaped vent eroded during an early explosive phase is filled with highly permeable pumice and ash. Gas loss through this permeable material then permits magma ascent without significant internal vapor overpressure. Another possible mechanism is the formation of fractures in overpressured magma (Stasiuk et al., 1996; Sparks, 1997; Jaupart, 1998). An important controlling parameter in either of these mechanisms is the ascent velocity of magma because slower rates of ascent result in greater time available for degassing (Jaupart and Allegre, 1991; Woods and Koyaguchi, 1994). For

example, Jaupart and Allegre (1991) suggested that a decrease in chamber overpressure during the course of an eruption would result in monotonic decrease in ascent velocity such that an initially explosive eruption grades into an effusive one. This process might have been important at Xitle because renewed explosive activity during the effusive phase is associated with a compositionally anomalous batch of magma (layer 3 andesitic inclusions). A magma mixing or recharge event could have caused an increase in overpressure in the magma storage reservoir beneath Xitle. This would increase ascent rates, decreasing the extent of gas loss during ascent so that the eruption became explosive again (Fig. 10). As this overpressure waned, the eruption switched back to an effusive style.

Gas is lost more easily from low viscosity basaltic magmas than from silicic magmas. In Hawaii, basaltic magma erupts as both lava fountains and lava flows. The lava flows involve highly degassed magma, but the primary water contents of undegassed magma are as high as 0.8 wt.% H_2O (Dixon et al., 1991; Wallace and Anderson, 1998). In order to account for low-pressure degassing in basaltic volcanoes, two mechanisms have been proposed. The first one (Dixon et al., 1991; Wallace and Anderson, 1998), observed in Hawaii, is degassing of lava in a surface lava lake followed by drainback of dense, degassed magma back down the conduit. The second process, inferred for Ozu-Oshima volcano in Japan (Kazahaya et al., 1994), is degassing related to convection of magma in the conduit. In this process magma degasses within the conduit, sinks because of the density increase caused by degassing, and then is mixed with undegassed magma at depth. This process was originally proposed to account for abundant gas emissions with little or no eruption of lava. Neither surface degassing or conduit convection processes can explain the eruption and degassing history at Xitle because the relatively small Xitle crater could not have contained a large lava lake and

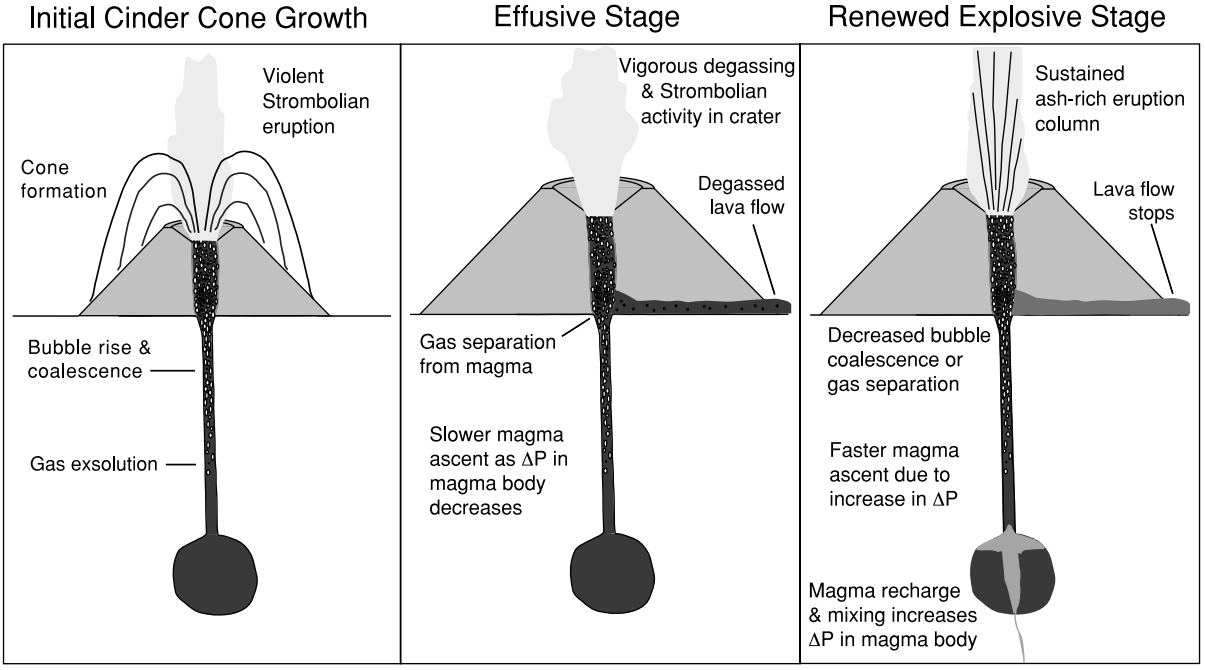

Fig. 10. Schematic model for explosive and effusive eruptions at Xitle as discussed in the text. The andesitic compositions of layer 3 melt inclusions and matrix glass suggest an association between magma recharge and the renewal of explosive activity. The recharging magma was more differentiated than typical Xitle basaltic magmas, so it would have been buoyant relative to basaltic magma in the subvolcanic magma body.

because the eruption involved a large volume of degassed lava.

One major difference between gas loss from silicic and basaltic magmas is that the low viscosity of the latter allows buoyant rise of gas bubbles through ascending magma (Wilson, 1980). The rate of bubble rise relative to magma is dependent on bubble size and magma viscosity (Parfitt and Wilson, 1995). Strombolian eruptions occur in low-viscosity magma when bubble rise is rapid relative to the magma so that rising bubbles coalesce (Wilson, 1980; Parfitt and Wilson, 1995). This results in discrete explosions that occur when large gas bubbles break at the surface. The normal to violent Strombolian eruptions (Walker, 1973) that construct scoria and cinder cones probably occur by this mechanism (Fig. 10), with the violence of the individual blasts being a complex function of the magma rise speed, viscosity, and volatile content (Head and Wilson, 1989). At both Parícutin and the 1995 eruption of Cerro Negro, Nicaragua, initial Strombolian eruptions formed cinder cones and were followed by increases in eruption intensity that were characterized by continuous ash-rich tephra columns that reached maximum altitudes of ~6 km and 2–2.5 km, respectively (Foshag and Gonzalez-Reyna, 1956; Bullard, 1962; Hill et al., 1998). These sustained eruptions contained greater proportions of ash than the Strombolian phase. The sustained eruptions probably resulted from higher magma ascent velocities such that gas bubbles remained entrained in rising magma and expanded until fragmentation, giving rise to a more continuous jet of gas and vesicular pyroclasts from the vent and an associated convecting column (Fig. 10). The Xitle tephra deposits that we have studied have similar areal distribution to tephra at Parícutin and were probably formed by a similar, sustained, ash-rich tephra column. At the opposite end of the spectrum, slow ascent rates may allow gas bubbles to migrate upwards so extensively that degassed magma erupts as lava flows. Krauskopf (1948) noted that, during lava effusion at Parícutin, vigorous gas emissions were confined entirely to the central vent of the cone whereas lava was emitted from near the base of the cone. He suggested that separation of gas from magma occurred continuously at shallow depths within the cone. This allowed degassed lava to flow laterally and exit near the base of the cone while gas escaped through bubbly magma in the uppermost part of the conduit just below the crater. A similar mechanism probably applies to degassing at Xitle, where the lower initial H_2O compared with Parícutin made it easier for magma to degas and erupt effusively (Fig. 10).

A surprising finding from our study of Xitle is that fully enclosed melt inclusions in the tephra deposits formed in magma that had undergone significant low-pressure degassing before inclusion entrapment. This seems contradictory because we infer that more rapid magma ascent rates were necessary to cause the explosive eruption that deposited the tephra. Olivine phenocrysts from the Xitle tephra have morphologies that range from equant skeletal (hopper) to polyhedral. Similar morphologies have been produced experimentally at cooling rates of 5–20°C/h and 2–10°C/h, respectively (Donaldson, 1976; Lofgren, 1981). Most of the Xitle olivines are <1 mm in size (Fig. 2). Using experimentally determined olivine growth rates for appropriate degrees of undercooling (Jambon et al., 1992), we estimate that olivines of this size and morphology could crystallize in about 3–30 h. Textural and melt inclusion evidence for rapid crystallization of olivine phenocrysts in response to shallow degassing has also been found at Stromboli volcano and cinder cones in the Pinacate volcanic field in northern Mexico (Gutmann, 1979; Metrich et al., 2001).

7. Summary

The 2000 yr BP eruption of Xitle volcano in central Mexico was largely effusive after an initial Strombolian cinder cone-building phase. However, a short-lived explosive phase of activity punctuated the eruption of lava flows and deposited three widespread tephra layers. Melt inclusions in olivine phenocrysts (Fo_{84-86}) from these three ash layers have dissolved H_2O concentrations that vary from 0.2 to 1.3 wt.%. The absence of detectable CO_2 in all but two inclusions combined with generally low S concentrations indi-

cates shallow-level degassing before olivine crystallization and melt inclusion formation. These results demonstrate that caution must be used when interpreting volatile data for melt inclusions because inclusions can form from strongly degassed melt. In the case of Xitle, effusive eruptions were the result of efficient degassing of magma during ascent. Most gas loss probably occurred through the top of the open vent as a result of bubble rise and gas separation in the magma column within the cone. Olivine morphologies are consistent with the interpretation that most crystal growth occurred at shallow depths as a result of water loss from the melt. The short-lived explosive phase at Xitle was associated with a compositionally anomalous batch of more andesitic magma, probably resulting from a magma mixing or recharge event. This likely increased the degree of overpressure in the magma storage reservoir, causing increased ascent rates and less time for degassing so that eruptions became explosive. As the overpressure waned, the eruption switched back to an effusive style once again.

Acknowledgements

We would like to thank Jamie Allan for many helpful discussions and for his assistance with fieldwork in Mexico. We also thank Hugo Delgado and Jorge Nieto-Obregon for their indispensable assistance with our fieldwork. We appreciate the help of Ray Guillemete with electron microprobe analyses and the financial support of the Department of Geology and Geophysics at Texas A&M University for the probe work. Thoughtful reviews by J. Gardner and T. Sisson and discussions with B. Hill helped us clarify our ideas and led to significant improvements in the final manuscript.

References

Anderson, A.T., Jr., 1973. The before eruption H_2O content of some high alumina magmas. Bull. Volcanol. 37, 530–552.

Anderson, A.T., Jr., 1991. Hourglass inclusions: theory and application to the Bishop rhyolitic tuff. Am. Mineral. 76, 530–547.

Anderson, A.T., Jr., Brown, G.G., 1993. CO_2 and formation pressures of some Kilauean melt inclusions. Am. Mineral. 78, 794–803.

Anderson, A.T., Jr., Newman, S., Williams, S.N., Druitt, T.H., Skirius, C., Stolper, E., 1989. H_2O, CO_2, Cl and gas in Plinian and ash-flow Bishop rhyolite. Geology 17, 221–225.

Bloomfield, K., 1975. A late-Quaternary monogenetic volcano field in central Mexico. Geol. Rundsch. 64, 476–497.

Bullard, F.M., 1962. Volcanoes: In History, In Theory, In Eruption. University of Texas Press, Austin, TX, 441 pp.

Cas, R.A.F., Wright, J.V., 1988. Volcanic Successions, Modern and Ancient. Unwin Hyman, London, 487 pp.

Cervantes, P., Molinero, R.J., 1995. Eventos volcanicos al sur de la ciudad de Mexico. B.S. Thesis, Facultad de Ingenieria, Universidad Nacional Autonoma de Mexico, Mexico DF, 74 pp.

Cervantes, P., 1999. Volatile contents in subduction-related basaltic magmas from Central Mexico: considerations on mantle enrichment processes and low pressure degassing during basaltic eruptions. M.S. Thesis, Department of Geology and Geophysics, Texas A&M University, College Station, TX, 97 pp.

Delgado, H., Arana-Salinas, L., Nieto-Obregon, J., Mendoza-Rosales, C., Silva-Romo, G., 1997. Pelado Volcano in southern Mexico City, a young monogenetic volcano ($<1{,}000$ years old) and its possible impact in human settlements (abstract). IAVCEI 1997, General Assembly, Puerto Vallarta, p. 123.

Delgado, H., Molinero, R.J., Cervantes, P., Nieto-Obregon, J., Lozano, R., Macias, H.L., Mendoza-Rosales, C., Silva-Romo, G., 1998. Geology of Xitle volcano in southern Mexico City: a 2000 year old monogenetic volcano in an urban area. Rev. Mex. Ci. Geol. 12, 115–131.

Demant, A., 1978. Caracteristicas del Eje Neovolcanico Transmexicano y sus problemas de interpretacion. Rev. Inst. Geol. U.N.A.M. 2, 172–188.

Dixon, J.E., Pan, V., 1995. Determination of molar absorptivity of dissolved carbonate in basanitic glass. Am. Mineral. 80, 1339–1342.

Dixon, J.E., Clague, D.A., 2001. Volatiles in basaltic glasses from Loihi seamount, Hawaii: Evidence for a relatively dry plume component. J. Petrol. 42, 627–654.

Dixon, J.E., Clague, D.A., Stolper, E.M., 1991. Degassing history of water, sulfur, and carbon in submarine lavas from Kilauea volcano, Hawaii. J. Geol. 99, 371–394.

Dixon, J.E., Stolper, E.M., 1995. An experimental study of water and carbon dioxide solubilities in Mid-Ocean Ridge basaltic liquids. Part II: applications to degassing. J. Petrol. 36, 1633–1646.

Dixon, J.E., Stolper, E.M., Holloway, J.R., 1995. An experimental study of water and carbon dioxide solubilities in Mid-Ocean Ridge basaltic liquids. Part I: calibration and solubility models. J. Petrol. 36, 1607–1631.

Dobran, F., 1992. Non-equilibrium flow in volcanic conduits and applications to the eruptions of Mt. St. Helens on May

18, 1980, and Vesuvius in AD 79. J. Volcanol. Geotherm. Res. 49, 285–311.
Donaldson, C.H., 1976. An experimental investigation of olivine morphology. Contrib. Mineral. Petrol. 57, 187–213.
Eichelberger, J.C., Carrigan, C.R., Westrich, H.R., Price, R.H., 1986. Non-explosive silicic volcanism. Nature 323, 598–602.
Eichelberger, J.C., 1989. Are extrusive rhyolites produced from permeable foam eruptions?: a reply. Bull. Volcanol. 51, 72–75.
Eichelberger, J.C., 1995. Silicic volcanism: ascent of viscous magmas from crustal reservoirs. Annu. Rev. Earth Planet. Sci. 23, 41–63.
Foshag, W.F., Gonzalez-Reyna, J.R., 1956. Birth and development of Parícutin volcano, Mexico. US Geol. Surv. Bull. 965D, 355–489.
Fries, C., Jr., 1953. Volumes and weights of pyroclastic material, lava, and water erupted by Parícutin volcano, Michoacán, México. Trans. Am. Geophys. Union 34, 603–616.
Giberti, G., Wilson, L., 1990. The influence of geometry on the ascent of magma in open fissures. Bull. Volcanol. 52, 515–521.
Gunn, B.M., Mooser, F., 1971. Geochemistry of the volcanics of Central Mexico. Bull. Volcanol. 34, 577–616.
Gutmann, J.T., 1979. Structure and eruptive cycle of cinder cones in the Pinacate volcanic field and the controls of Strombolian activity. J. Geol. 87, 448–454.
Head, J.W.III., Wilson, L., 1987. Lava fountain heights at Pu'u O'o, Kilauea, Hawaii: Indicators of amount and variations of exsolved magma volatiles. J. Geophys. Res. 92, 13715–13719.
Head, J.W.III., Wilson, L., 1989. Basaltic pyroclastic eruptions: Influence of gas-release patterns and volume fluxes on fountain structure, and the formation of cinder cones, spatter cones, rootless flows, lava ponds and lavas flows. J. Volcanol. Geotherm. Res. 37, 261–271.
Hill, B.E., Connor, C.B., Jarzemba, M.S., La Femina, P.C., Navarro, M., Strauch, W., 1998. 1995 eruptions of Cerro Negro volcano, Nicaragua, and risk assessment for future eruptions. Geol. Soc. Am. Bull. 110, 1231–1241.
Houghton, B.F., Wilson, C.J.N., Smith, I.E.M., 1999. Shallow-seated controls on styles of explosive basaltic volcanism: a case study from New Zealand. J. Volcanol. Geotherm. Res. 91, 97–120.
Ihinger, P.D., Hervig, R.L., McMillan, P.F., 1994. Analytical methods for volatiles in glasses. In: Carroll, M.R., Holloway, J.R. (Eds.), Volatiles in Magmas. Mineral. Soc. Am. Rev. Mineral. 30, 67–121.
Jambon, A., Lussiez, P., Clocchiatti, R., Weisz, J., Hernandez, J., 1992. Olivine growth rates in a tholeiitic basalt: an experimental study of melt inclusions in plagioclase. Chem. Geol. 96, 277–287.
Jaupart, C., 1998. Gas loss from magmas through conduit walls during eruption. In: Gilbert, J.S., Sparks, R.S.J. (Eds.), The Physics of Explosive Volcanic Eruptions. Geol. Soc. London Spec. Publ. 145, 73–90.
Jaupart, C., Allegre, C.J., 1991. Gas content, eruption rate and instabilities of eruption regime in silicic volcanoes. Earth Planet. Sci. Lett. 102, 413–429.
Kazahaya, K., Shinohara, H., Saito, G., 1994. Excessive degassing of Izu-Oshima Volcano. Bull. Volcanol. 56, 207–216.
Krauskopf, K., 1948. Mechanism of eruption at Parícutin volcano, Mexico. Geol. Soc. Am. Bull. 59, 711–731.
Lofgren, G., 1981. Experimental studies on the dynamic crystallization of silicate melts. In: Hargraves, R.B. (Ed.), Physics of Magmatic Processes. Princeton University Press, Princeton, NJ, pp. 487–551.
Lowenstern, J.B., 1995. Applications of silicate-melt inclusions to the study of magmatic volatiles. In: Thompson, J.F.H. (Ed.), Magmas, Fluids, and Ore Deposits. Mineral. Assoc. Canada Short Course 23, 71–99.
Luhr, J.F., 2001. Glass inclusions and melt volatile contents at Parícutin Volcano, Mexico. Contrib. Mineral. Petrol. 142, 261–283.
Macdonald, G.A., Katsura, T., 1964. Chemical compositions of Hawaiian lavas. J. Petrol. 5, 82–133.
Mackwell, S.J., Kohlstedt, D.L., 1990. Diffusion of hydrogen in olivine: implications for water in the mantle. J. Geophys. Res. 95, 5079–5088.
Martel, C., Pichavant, M., Bourdier, J.-L., Traineau, H., Holtz, F., Scaillet, B., 1998. Magma storage conditions and control of eruption regime in silicic volcanoes: experimental evidence from Mt. Pelée. Earth Planet. Sci. Lett. 156, 89–99.
Martin del Pozzo, A.L., 1982. Monogenetic volcanism in the Sierra Chichinautzin, Mexico. Bull. Volcanol. 45, 9–29.
Metrich, N., Bertagnini, A., Landi, P., Rosi, M., 2001. Crystallization driven by decompression and water loss at Stromboli Volcano (Aeolian Islands, Italy). J. Petrol. 42, 1471–1490.
Mooser, F., Nairn, A.E.M., Negendank, J.F.W., 1974. Palaeomagnetic investigations of the Tertiary and Quaternary igneous rocks: VIII. A palaeomagnetic and petrologic study of volcanics of the Valley of Mexico. Geol. Rundsch. 63, 451–483.
Nakamoto, K., 1978. Infrared and Raman Spectra of Inorganic and Coordination Compounds, 3rd edn. John Wiley, New York, 448 pp.
Newman, S., Epstein, S., Stolper, E.M., 1988. Water, carbon dioxide, and hydrogen isotopes in glasses from the ca. 1340 A.D. eruption of the Mono Craters, California: constraints on degassing phenomena and initial volatile content. J. Volcanol. Geotherm. Res. 35, 75–96.
Parfitt, E.A., Wilson, L., 1995. Explosive volcanic eruptions-IX. The transition between Hawaiian-style lava fountaining and Strombolian explosive activity. Geophys. J. Int. 121, 226–232.
Roedder, E., 1965. Liquid CO_2 inclusions in olivine-bearing nodules and phenocrysts from basalts. Am. Mineral. 50, 1746–1782.
Roedder, E., Fluid Inclusions. Rev. Mineral., Mineral. Soc. Am. 12, 1984.
Roedder, P.L., Emslie, R.F., 1970. Olivine-liquid equilibrium. Contrib. Mineral. Petrol. 29, 275–289.

Roggensack, K., Hervig, R.L., McKnight, S.B., Williams, S.N., 1997. Explosive basaltic volcanism from Cerro Negro volcano: influence of volatiles on eruptive style. Science 277, 1639–1642.

Siebe, C., 2000. Age and archaeological implications of Xitle volcano, southwestern Basin of Mexico-City. J. Volcanol. Geotherm. Res. 104, 45–64.

Sisson, T.W., Bronto, S., 1998. Evidence for pressure-release melting beneath magmatic arcs from basalt at Galunggung, Indonesia. Nature 391, 883–886.

Sisson, T.W., Layne, G.D., 1993. H_2O in basalt and basaltic andesite glass inclusions from four subduction-related volcanoes. Earth Planet. Sci. Lett. 117, 619–635.

Sobolev, A.V., Chaussidon, M., 1996. H_2O concentrations in primary melts from supra-subduction zones and mid-ocean ridges: Implications for H_2O storage and recycling in the mantle. Earth Planet. Sci. Lett. 137, 45–55.

Sparks, R.S.J., 1997. Causes and consequences of pressurization in lava dome eruptions. Earth Planet. Sci. Lett. 150, 177–189.

Stasiuk, M.V., Barclay, J., Carroll, M.R., Jaupart, C., Ratté, J.C., Sparks, R.S.J., Tait, S.R., 1996. Degassing during magma ascent in the Mule Creek vent (USA). Bull. Volcanol. 58, 117–130.

Swanson, D.A., Fabbi, B.P., 1973. Loss of volatiles during fountaining and flowage of basaltic lava at Kilauea Volcano, Hawaii. J. Res. US Geol. Surv. 1, 649–658.

Walker, G.P.L., 1973. Explosive volcanic eruptions – a new classification scheme. Geol. Rundsch. 62, 431–446.

Wallace, P.J., Carmichael, I.S.E., 1994. Sulfur speciation in submarine basaltic glasses as determined by measurements of S$K\alpha$ X-ray wavelength shifts. Am. Mineral. 79, 161–167.

Wallace, P.J., Gerlach, T.M., 1994. Magmatic vapor source for sulfur dioxide released during volcanic eruptions: evidence from Mount Pinatubo. Science 265, 497–499.

Wallace, P.J., Anderson, A.T., Jr., 1998. Effects of eruption and lava drainback on the H_2O contents of basaltic magmas at Kilauea Volcano. Bull. Volcanol. 50, 327–344.

Wallace, P.J., Carmichael, I.S.E., 1999. Quaternary volcanism near the Valley of Mexico: implications for subduction zone magmatism and the effects of crustal thickness variations on primitive magma compositions. Contrib. Mineral. Petrol. 135, 291–314.

Wallace, P.J., Anderson, A.T., Jr., Davis, A.M., 1995. Quantification of pre-eruptive exsolved gas contents in silicic magmas. Nature 377, 612–616.

Watson, E.B., 1994. Diffusion in volatile-bearing magmas. In Carroll, M.R., Holloway, J.R. (Eds.), Volatiles in Magmas. Mineral. Soc. Am. Rev. Mineral. 30, 371–411.

Westrich, H.R., Stockman, H.W., Eichelberger, J.C., 1988. Degassing of rhyolitic magma during ascent and emplacement. J. Geophys. Res. 93, 6503–6511.

Westrich, H.R., Eichelberger, J.C., Hervig, R.L., 1991. Degassing of the 1912 Katmai magmas. Geophys. Res. Lett. 18, 1561–1564.

Westrich, H.R., Eichelberger, J.C., 1994. Gas transport and bubble collapse in rhyolitic magma: an experimental approach. Bull. Volcanol. 56, 447–458.

Wilson, L.J., 1980. Relationship between pressure, volatile content and ejecta velocity in three types of volcanic explosions. J. Volcanol. Geotherm. Res. 8, 297–313.

Wilson, L., Sparks, R.S.J., Walker, G.P.L., 1980. Explosive volcanic eruptions IV. The control of magma properties and conduit geometry on eruption column behaviour. Geophys. J. R. Astron. Soc. 63, 117–148.

Wood, C.A., 1980. Morphometric evolution of cinder cones. J. Volcanol. Geotherm. Res. 7, 387–413.

Woods, A.W., Koyaguchi, T., 1994. Transitions between explosive and effusive eruptions of silicic magmas. Nature 370, 641–644.